

Landslides (2023) 20:25–38
 DOI 10.1007/s10346-022-01955-y
 Received: 2 May 2022
 Accepted: 3 August 2022
 Published online: 30 August 2022
 © Springer-Verlag GmbH Germany,
 part of Springer Nature 2022,

Gang Luo  · Xinan Chen · Qian Zhang · Kun He · Maolin Wu · Weigang Shen · Bo Liu



Failure mechanism and sedimentary characteristics of a catastrophic rockslide avalanche induced by the 2008 Wenchuan earthquake

Abstract The infrastructure construction in tectonically active mountainous areas is faced with the threat of earthquake-induced rockslide-avalanches. We took the Woqian rockslide-avalanche induced by the Wenchuan earthquake near the Qinchuan active fault, Southwestern China as an instance to elucidate a unique initiation mechanism of the inward inclined bedding slope, which had a characteristic of twice destabilization in succession. The high-resolution satellite images, UAV aerial photography, field investigation, and numerical simulation were conducted to reveal the failure processes. The results suggested that (1) the long-term headward erosion of the gully runoff had locally exposed the unconformity contact plane within the strata, which evolved as a part of the sliding plane; (2) the seismic loading produced a rapid shear strain increment on the unconformity plane; (3) the brittle rupture occurred along the sliding plane at the bottom of the sliding source I developed at 6 s after the seismic wave arrival; (4) as a “resistance barrier”, the sliding source I first collapsed and most of it accumulated at a short distance; (5) the sliding source II subsequently slid along the apparent dip of the bedding plane and then entrained the deposits of the source I into a catastrophic rock avalanche. The failure mechanism of such carbonaceous bedding slopes with similar geological conditions could provide an insight into the early risk recognition of potential rockslides and the safe site selection of infrastructures.

Keywords Earthquake-induced rockslide · Rockslide-avalanche · Failure mechanism · Carbonate rock · Finite difference method

Introduction

As one type of highly energetic and dangerous geological disaster, co-seismic rockslide-avalanches in alpine-canyon areas are extremely dangerous in terms of huge volume, tremendously high velocity, and long-runout (Keefer 1984; Hungr 2006; Pudasaini and Miller 2013; Wang et al. 2013; Liu et al. 2020). In Sichuan Province, China, the co-seismic rock avalanches induced by the M 7.9 Wenchuan earthquake on 12th May 2008 caused severe casualties and property losses within 20 km distance of the seismogenic Longmenshan thrust fault (Qi et al. 2010; Gorum et al. 2011).

Previous work attributed the failure of co-seismic rockslides to groundwater (Wang et al. 2013), geology (Roback et al. 2018; He et al. 2021), structural features of rock masses (Hungr et al. 2014; Stead and Wolter 2015; Wang et al. 2021; He et al. 2022), direct thrust force

of the hanging wall of seismogenic faults (Dai et al. 2011), energy release along with co-seismic surface ruptures (Xu and Xu 2014; Kargel et al. 2016; Gombert et al. 2019; Vanani et al. 2021), strong seismic acceleration (Sun et al. 2011; Kargel et al. 2016; Wang et al. 2019b), wave amplification effect (Mahani and Kazemian 2018; Wang et al. 2018), or progressive seismic fatigue of rock masses (Oswald et al. 2021). However, due to the complicated geological environmental setting and various influencing factors, the failure mechanisms of co-seismic rockslides are very different and still poorly understood (Petley 2013; Fan et al. 2019; Wang et al. 2020; Zhang et al. 2021). Probing into the failure mechanism of rockslide for specific areas is a prerequisite for risk area zoning, appropriate precautions, possible mitigating strategies and proper treatment (Pudasaini and Miller 2013; Lin et al. 2018; Wang et al. 2019a; Zhang et al. 2021).

With the development of numerical simulation technologies, the dynamic response and failure process of co-seismic rockslides have been studied in detail by means of the finite difference method (FDM) and discrete element method (DEM) (Yin et al. 2015; Liu et al. 2020). The FDM involving FLAC3D has the ability to simulate the progressive rupture without any prior assumptions about where and how a crack and failure will occur (Gong and Tang 2017). The DEMs involving the DDA, 3DEC and PFC3D can reflect the characteristics of large deformation, fragmentation and flow occurring in the sliding process (Fan et al. 2019; Lin et al. 2019; Zhang et al. 2019, 2021). However, the critical sliding plane was not easily determined by the DEMs, which required exact constructions and local densification of the structural planes (Liu et al. 2020). FLAC3D software with explicit Lagrangian algorithm and hybrid discrete partition technique can accurately simulate the plastic failure of rock masses and rapidly judge the position of the critical sliding plane (Yin et al. 2015). Promisingly, the discontinuous deformation and displacement (DDD) method can capture the whole slope-failure process, including not only the crack initiation, propagation, and coalescence processes in the small deformation stage but also the block movement in the large displacement stage (Gong and Tang 2017).

In this study, the characteristics of the Woqian rockslide-avalanche (WRA) located in western Sichuan triggered by the 2008 Wenchuan earthquake are presented. Field investigations were performed to determine the geological setting and the deposits geomorphology on March 2010 and January 2011. Optical satellite images and unmanned aerial vehicle were selected to obtain high resolution images and produce the zoning of the WRA. The numerical simulation by FLAC3D

was conducted to explore the initial deformation and failure process of the sliding planes subjected to the seismic load. The knowledge learned from this case, indeed, provides an insight on the site selection and early warning against the co-seismic rockslide-avalanches.

Methods

Visual interpretation based on satellite images

Firstly, the pre- and post-sliding topographical evolution of the rockslide (1 February 2006 and 26 December 2009) was analyzed by high-resolution satellite images with 5 m resolution from Google Earth. For instance, the area of the main scarp and the sliding plane, the eroded grooves and the boundary of the deposits can be accurately obtained from the images. Additionally, the digital elevation model of the numerical simulation was established based on elevation data.

UAV and field surveys

Secondly, the sliding plane, streaks on the exposed bedrock of the main scarp and deposit characteristics along the path were investigated by UAV aerial photography and field investigation. Thirdly, the statistical analysis of particle sizes on the surface of the deposits along the flow path was carried out by the tapeline measurement and image recognition technology.

Numerical simulation by FLAC3D

Based on topographic data before the landslide and mechanics parameters tests of the rock, the geological model of slope is established by FLAC3D (Itasca Consulting Group, Inc 2018) to simulate the failure process of the WRA. The different groups represent the sliding masses and the bedding rock, which are separated by the sliding plane composing of the unconformity contact

plane, bedding plane and tensile scarp. Continuum materials in the model are considered to behave as elastic-perfectly-plastic. The Mohr–Coulomb criterion is applied to control the failure envelope of the rock masses and the sliding plane. The seismic accelerations with 0.02 s intervals and 150 s duration obtained from the nearest seismograph station were used as input data. The local damping ratio of the model is arranged as 0.05.

Study area

Overview of the WRA

Induced by the Wenchuan Earthquake, the $12 \times 10^6 \text{ m}^3$ Woqian rockslide avalanche (WRA) with a geographic coordinate of 104.9596 E, 32.3060 N, originated near the mountain summits, transported 2050 m along the sinuous gully and ultimately destroyed the Woqian village, causing 38 deaths (Tang et al. 2011; Dai et al. 2011). The WRA is situated on the Shikan fault as a western branch of the Qingchuan fault (Figs. 1 and 2), which is a NE strike slip-thrust fault with a dip angle of 60° . Activated by the Wenchuan earthquake, a 60-km-long surface rupture along the Shikan fault characterized by road dislocation, water-gushing, sand liquefaction and intensively distributed landslides was produced (Sun et al. 2015). Compared with the landslide distribution along the two faults, the concentrated release of strain energy stored in the rock mass along the surface rupture was considered as a crucial factor triggering the WRA (Fig. 2). The monitoring station in Hanzeng town, 64 km away from the WRA, measured the peak ground accelerations during the earthquake as 519.5 gal (east–west), 350.1 gal (north–south) and 444.3 gal (up–down).

Geomorphologic characteristics of the WRA

The geomorphological pattern of the rockslide area was the alpine-gorge landscape. Before the WRA, the Woqian village was located

Fig. 1 Location of the WRA, approximately 211 km from the epicenter

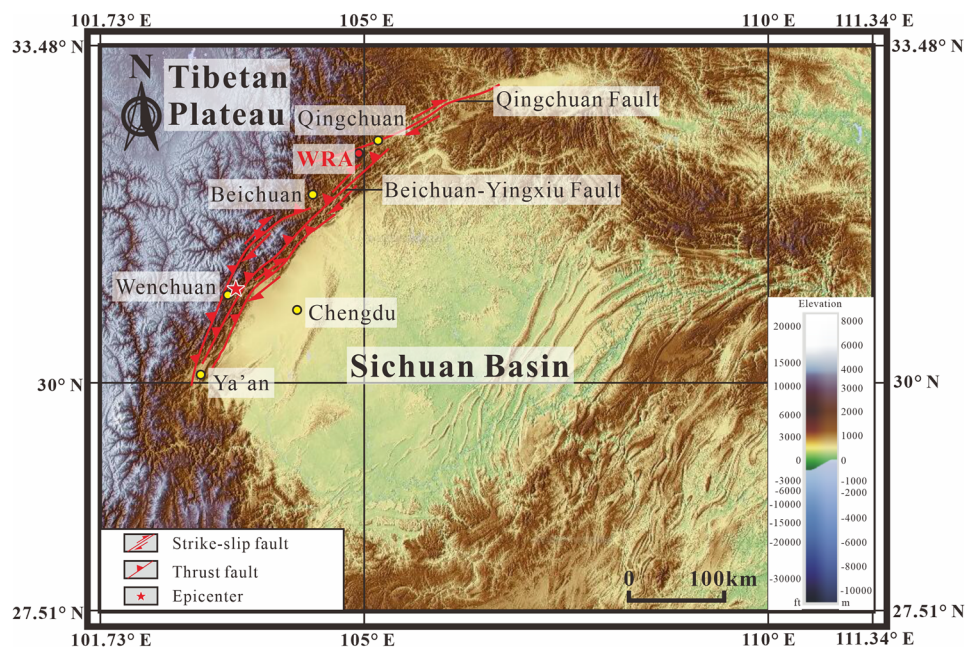
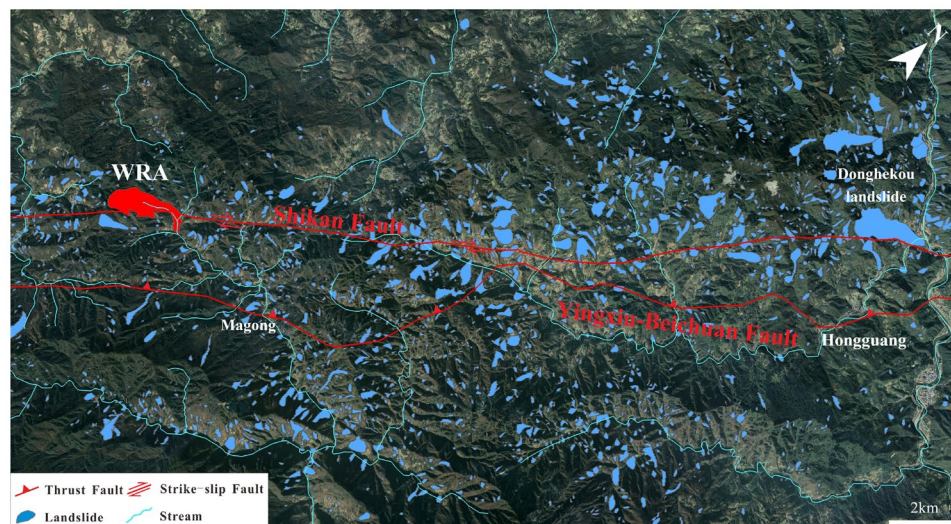


Fig. 2 Densely distributed landslides along the 60 km surface rupture of the Shikan fault. The landslide inventory is derived from Xu et al. (2014)



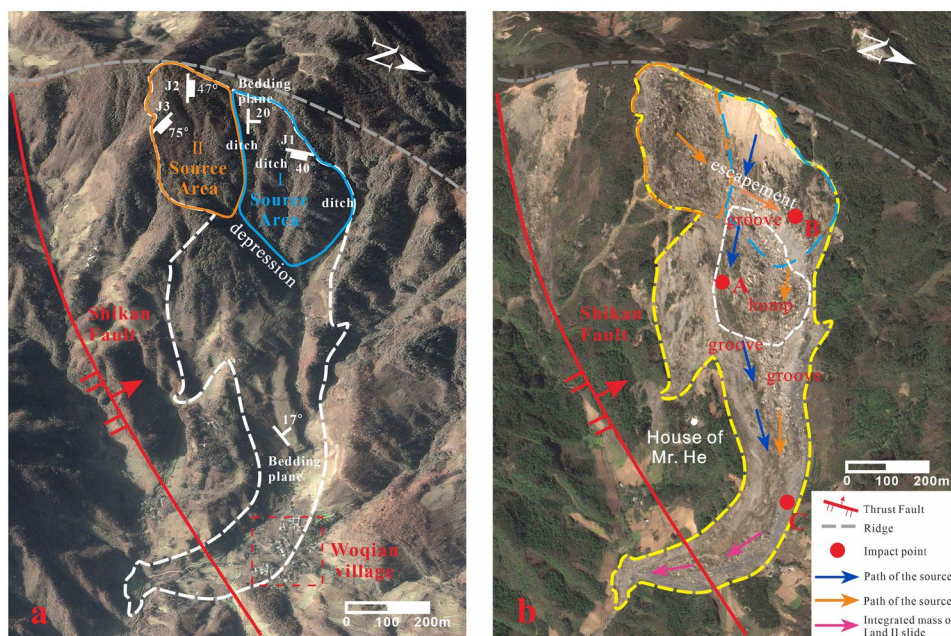
at the gentle outlet of the sinuous gully (Fig. 3a). The elevations of the watershed and outlet of the gully were 1875 m and 1270 m respectively with a relative elevation difference of 605 m. The slope was covered with dense vegetation and had no obvious crack on the slope surface. The source area of the WRA from 1590 m to 1875 m was the upper catchment area of the gully, which was deeply incised by ditches and tightly constricted by lateral mountain ridges (Fig. 3a). After the two sources of the WRA sequentially initiated from the east-facing steep slope near the summits, a chair-like main scarp approximated 60° along while a N–S trending ridge was produced (Fig. 3b).

The plane shape of the WRA was like “silver carp”, which can be chopped up into the source area, scattering area, acceleration area, transportation area and accumulation area from top to bottom (Fig. 4). The whole horizontal travel distance of the WRA was about

2050 m, the vertical drop was 605 m, the equivalent coefficient of friction was 0.22 (Fig. 5). The area of deposits was about $6 \times 10^5 \text{ m}^2$, the average thickness was about 20 m, and the total volume was about $12 \times 10^6 \text{ m}^3$. The thickness and the gradient of the deposits in different areas are shown in Table 1.

According to Table 1, the thickness and the slope of deposits in the sources area were maximum and second-lowest respectively, which is very different from the thicker tendency of the deposits from the source to the terminus of the co-seismic rockslide avalanches during the Wenchuan earthquake, such as the Daguangbao landslide (Cui et al. 2021), Donghekou landslide (Sun et al. 2011), Wenjiagou landslide (Zhang et al. 2016) and Xiejiadianzi landslide (Dai et al. 2011). It was inferred that the sliding masses were partly blocked after initiation or the slide masses accumulated twice on the source area. Namely, the rock masses of the source I were

Fig. 3 Pre- and post-event satellite imagery of the WRA with a resolution of 5 m (© Google Earth). **a.** initial topography of linear fault valley and compressive ridges before the WRA, joint set J1 (dip 40°, dip direction 80°) subparallel to the N-S mountain ridge became the rear boundary of the sliding source. **b.** distribution characteristics of the deposits of the WRA and two lateral deep-cutting grooves along the gully showing two sliding paths



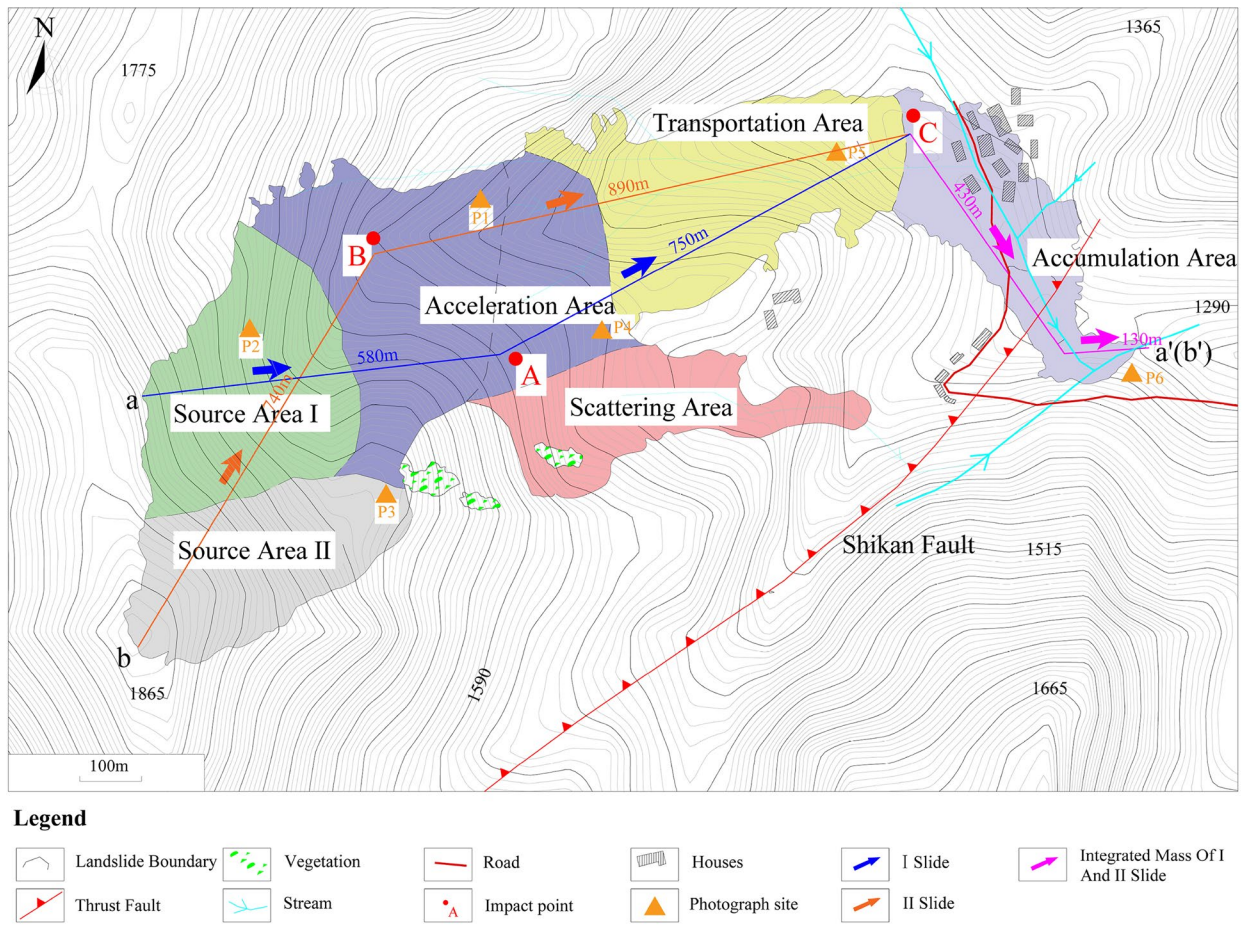


Fig. 4 Zones of the WRA and the two sliding paths: the blue and the orange arrows respectively represent the sliding route of the source I and II

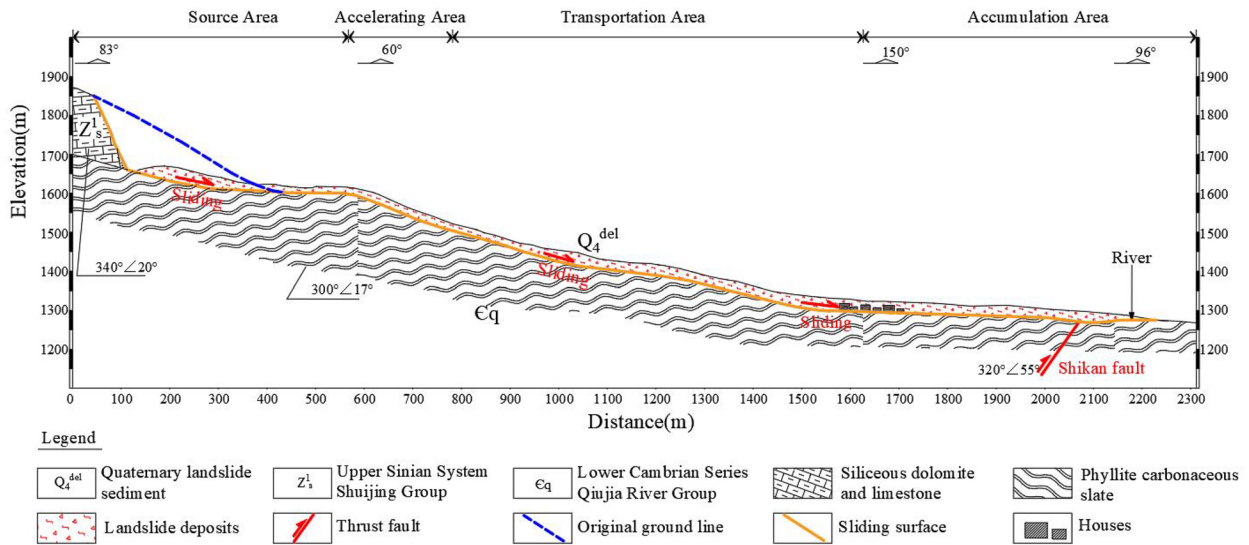


Fig. 5 Geological profile (a-a') of the WRA (modified after Tang et al. 2011)

Table 1 Terrain features of the deposits of the WRA

| Motional area | Length (m) | Width (m) | Elevation (m) | Thickness of deposit (m) | Slope of deposit (°) |
|---------------------|------------|-----------|---------------|--------------------------|----------------------|
| Source area | 500 | 470 | 1630–1870 | 10–30 | 7 |
| Scattering area | 400 | 160 | 1500–1600 | 5–10 | 18 |
| Acceleration area | 450 | 350 | 1500–1630 | 14–17 | 22 |
| Transportation area | 550 | 250 | 1370–1500 | 14–27 | 11 |
| Accumulation area | 550 | 170 | 1270–1370 | 14–23 | 4 |

momentarily stopped during collision with the topographic depression and deposited at the scarp toe. The rock masses of the source II subsequently destabilized and entrained the deposits.

Stratum and lithology

Through the field investigation, the stratum from the top to the bottom in the WRA area is siliceous dolomite and limestone belonging to the Shuijing Formation of the Sinian period (Z_s^1) and phyllite and siliceous slate belonging to the Qiujiuhe Formation of Cambrian period (ϵq). The two strata have a parallel unconformity contact. The bedding plane and two joint sets of phyllite and siliceous slate were $300^\circ \angle 17^\circ$, $183^\circ \angle 62^\circ$ and $85^\circ \angle 87^\circ$ respectively. The bedding plane and three joint sets of the limestone were $340^\circ \angle 20^\circ$ (inward slope), $80^\circ \angle 40^\circ$, $340^\circ \angle 47^\circ$ and $56^\circ \angle 75^\circ$ respectively (Fig. 3a). Due to the tectonic compression and the weathering, the siliceous dolomite and limestone on the main scarp appeared very fragmented and the unloading fractures densely developed.

According to the lithology observation of the deposits, it was found that the deposits primarily consisted of a large amount of siliceous limestone and a small amount of phyllite (Tang et al. 2011; Dai et al. 2011). It is worth mentioning that the siliceous limestone can easily break up along the structural planes to be sheet or chunk by a hammer (Fig. 6a), but the phyllite with thin-layer structure did not react in the same way (Fig. 6b).

Geomorphic characteristics of the WRA

Source area

The source area with 1590–1875 m in elevation can be divided into I and II areas based on the discontinuous step-shaped sliding

Fig. 6 Lithology of the deposits. **a** Angular fragmented siliceous dolomite and limestone on the surface of the deposits, which can be easily broken into chunks or thin layers by a hammer. **b** Phyllite with higher strength sporadically distributed on the surface of the deposits, accounting for 5% of the deposit area



planes and scarps (Fig. 7). According to the vertical striations on the bedrock in the middle of the source area I (Fig. 8a), it was inferred that the source I firstly collapsed downwards under the strong earthquake. The sliding plane of the source I could be the unconformity contact interface of the limestone and phyllite

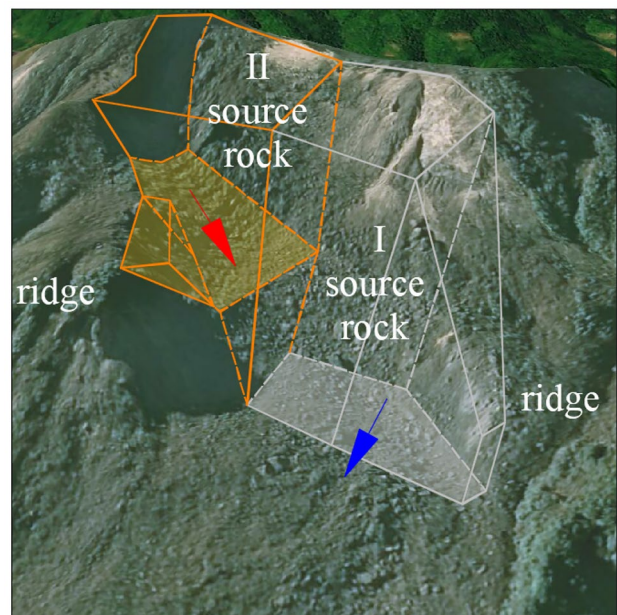
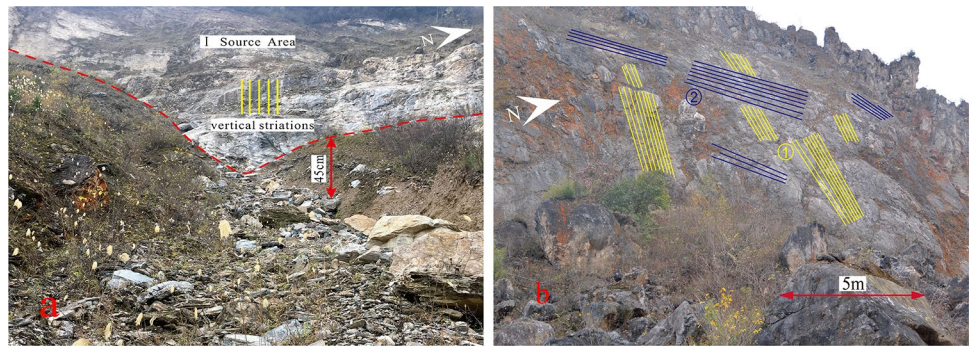


Fig. 7 Failure mechanism of the sources I and II. The sliding directions of the sources were the inclination of the unconformity contact interface and the apparent dip of the limestone strata respectively. The source I as a “key resistance block” determined the overall stability of the WRA

Fig. 8 Main scarp of the WRA (camera position P2 in Fig. 4). **a** Vertical striations (yellow lines) on the bedrock of the source area I indicating the sliding direction of the source I. **b** Inclined striations (blue lines) on the bedrock of the source area I indicating the sliding direction of the source II

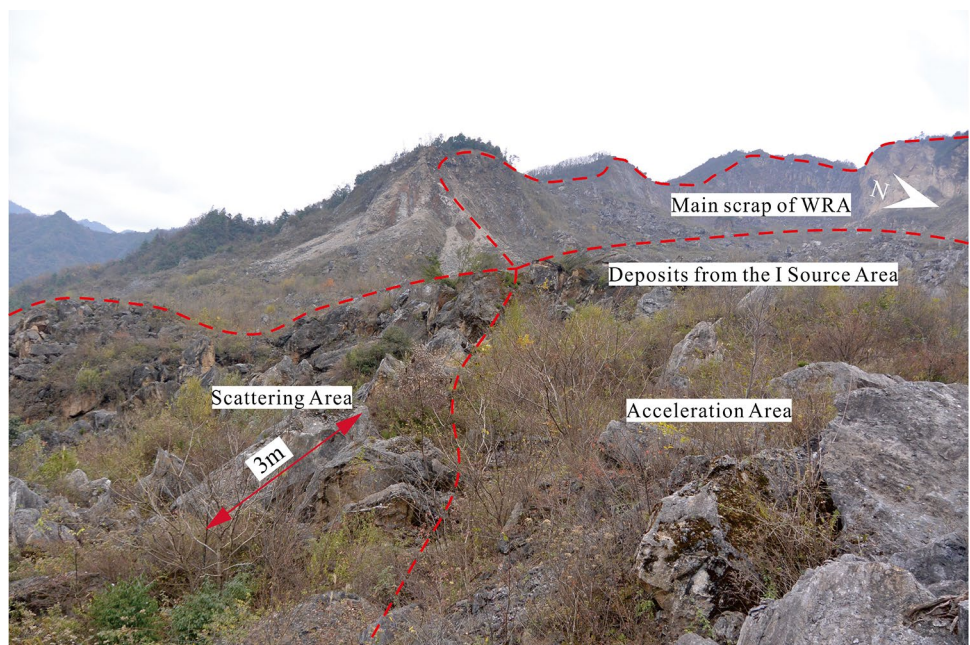


(Fig. 5). The main scarp of the source area I was 180 m high and 500 m wide with the occurrence of $90\text{--}120^\circ \angle 53\text{--}65^\circ$, which developed from the joint set J₁ and unloading fissures. According to the inclined striations on the smooth bedrock at the right part of the source area I (Fig. 8b), it was inferred that the source II slid along the apparent dip of the limestone bedding plane and rubbed the main scarp of the source area I. The main scarp of the source II was 160 m high and 370 m wide with the occurrence of $340^\circ \angle 47^\circ$ (Fig. 3).

Scattering area

The scattering area was located on the slope of the right ridge beyond the gully (Figs. 3b and 4). Due to the low-intensity collision between the low-velocity and relatively intact sliding masses from the sliding source I and the right ridge, large-size rock fragments were produced and distributed on the scattering area and the upper stream of the acceleration area (Fig. 9). Significantly, because of the barrier effect of the right ridge, the volume and total kinetic energy of the sliding masses reduced to some extent.

Fig. 9 The sliding masses scraped the crown of the right mountain ridge and scattered on another side slope (camera position P4 in Fig. 4)



Acceleration area

The post-landslide topography of the acceleration area was characterized by an armoured hump in the middle and two new-emerged grooves on both sides, which was possibly produced by the fierce entrainment of the sliding masses (Fig. 3b). On the hump, the original stratigraphic structure was well-preserved and the fragments with a diameter of 2–5 m accounted for approximately 53% area (Figs. 9 and 10). The two deep incised grooves were covered by relatively finer particles (0.1–1 m).

The phenomenon that the left groove was deeper than the right one indicated the sliding masses from the source II possessed greater sliding velocity, impact energy and erosional competence. Significantly, given the multiple collisions between the sliding masses and gully banks, the rockslide was pulverized and transformed into a rapid rock avalanche. The sliding direction of the sliding masses from the source I turned to 60°NE from the initial 85°NE after impacting with point A (Fig. 3b). The sliding direction of the sliding masses from the source II turned to 70°NE from the initial 40°NE after impacting with point B (Fig. 3b).

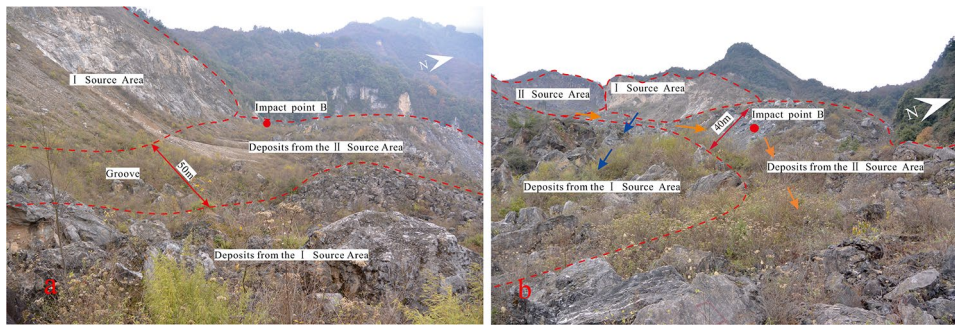


Fig. 10 Geomorphic characteristics of the WRA. **a** A 50 m wide groove produced by the scouring and entraining the sliding masses from the source II (camera position P3 in Fig. 4). **b** A hump in the

middle of the deposits and a new-generated groove on the left; the blue and the orange arrows respectively represent the two sliding paths (camera position P1 in Fig. 4)

Transportation area and accumulation area

The geomorphic characteristics of the transportation area were the same as the acceleration area (Fig. 10a). Controlled by the narrowing topography of the gully, the two sliding masses converged rapidly and further fragmented. As a result, the avalanche squeezed out the narrow section toward point C (Fig. 4) leaving obvious striations on the gully banks (Fig. 11a). Additionally, an NNE-trending linear escarpment in the deposits from the source I, just perpendicular to the sliding path (Fig. 11a), was generated by the erosion of the sliding masses from the source II.

The accumulation area was the residential area of the Woqian village, which was not spared as the high-speed avalanche exceeded super-elevation in the gully bend. Because of the entrainment and fragmentation of the avalanche, the fine-particle proportion of the deposits in the accumulation area was higher than the one in other areas. It is noteworthy to mention that blocks with diameters greater than 3 m appeared on the surface of the deposits underlain by much finely fragmented debris (Fig. 11b).

Particle size of the surficial deposits

Although the morphological features, such as surface landforms and deposit size order, are significant for revealing the transportation mechanism and the fragmentation degree of the rock avalanches, opportunities to closely examine the internal fragments are impossible. Alternatively, the particle size on the deposits' surface

can provide an insight into the degree of fragmentation. According to the statistical results at different sites by careful measurements (Fig. 12), abundant granular fragments appeared at the collision points and the deposits rarely well-preserved original stratigraphic sequence. As shown in Fig. 12, the boulders larger than 1 m at the points S1, S2, S3, S4, S5, S6 accounted for 91.0%, 74.9%, 52.5%, 63.9%, 80.5% and 27.5% respectively.

Comparing the particle sizes of the surface deposits at the points S1 and S2 (Fig. 12), the relatively short sliding distance of the source I and the barrier of the original depression (Fig. 3a) produced lower fragmentation degree at the point S1. Therefore, a hump covered by large boulders was formed at the proximal end (Fig. 3b). The enlarged gravity energy of the source II due to the generated cliff after the detachment of the source I and the larger impact angle aligned with the sliding plane of the source II (Fig. 7) can be responsible for the intense fragmentation at the point S2. By comparing the particle size distribution of the deposits at points S3 and S4 with the similar sliding distance (Fig. 12), the smaller the impact angle (the angle between the sliding direction and the normal direction), the higher the degree of fragmentation.

Over all, with the increase of the sliding distances of the source I (S1-S4-S6) and the source II (S2-S3-S6), the fragments smaller than 1 m gradually increased and the fragments larger than 1 m gradually reduced (Fig. 12). Notably, sudden increase of the diameter of the fragments at the point S5 (Fig. 12) could be caused by the rapid convergence of two avalanches at the narrow section of the gully and sieving effect of the undulant ground (Wang

Fig. 11 Accumulative characteristics of the WRA. **a** Striations on the gully banks (camera position P5 in Fig. 4). **b** Blocks with diameters greater than 3 m at the trimline of the deposits (imaged by Qingchuan Land Bureau, P6 in Fig. 4)

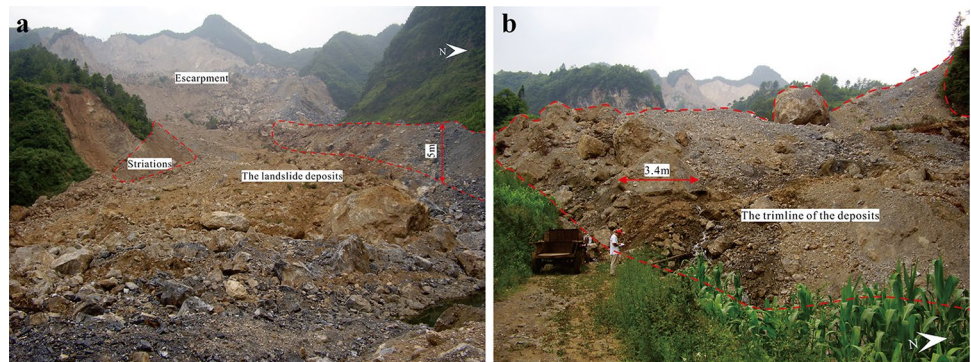
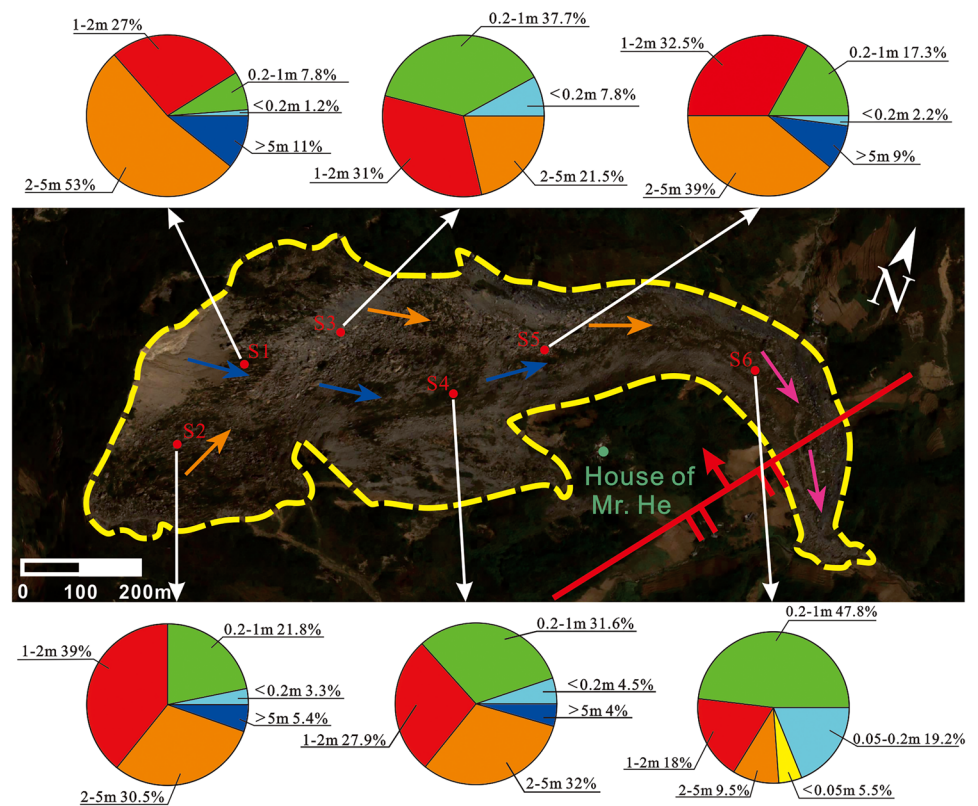


Fig. 12 Sampling positions and proportion of particle size on the deposits' surface, which indicated the fragmentation degree



et al. 2015). The topographic jamming effect at the narrow gully could cease a portion of the large fragments (Huang et al. 2021) and the vibration-induced sieving could push the large fragments upwards on the deposit surface. Therefore, the combined action of the shear-induced and impact-induced fragmentation can be as a reasonable explanation for the particle size distribution of the deposit (Zhang et al. 2019).

According to the discontinuous step-shaped sliding planes (Fig. 7), the different occurrences of striae on the bedrock in the main scarp scratched by the sliding masses (Fig. 8), the eroded flowing paths in the high-resolution satellite image ((Fig. 3b), the topography characteristics of the deposits (Fig. 12), the failure mechanism of the source was speculated as a twice destabilization in tandem with several seconds interval. The source I destabilized along the unconformity contact interface induced by the strong seismic force. The source II subsequently caused an apparent dip sliding along the inclined bedding plane because of the traction of the destabilized source I and the ongoing seismic force.

Numerical simulation of the WRA

The model with 1600 m length, 1050 m width and 625 m height was constructed by FLAC_{3D} based on the aerial survey data (Fig. 13). The group in purple, red and blue represents source I, source II, and sliding bed, respectively. The model was discretized into 139,604 tetrahedral elements. The bottom of the model is a static boundary and the four sides are free field boundaries. The seismic accelerations (Fig. 14) are decomposed and synthesized along with the

strike and dip directions of the slope. The mechanical parameters of limestone (sliding masses) are shown in Fig. 15 and Table 2. Because the Mohr–Coulomb strength criterion can reflect the shear failure and tensile failure of the rock masses under the seismic loading, it was adopted to simulate the geomechanical behavior and failure modes of the sliding masses and sliding plane. According to Mohr's circle graphic method, the shear stress τ and the normal compressive stress σ can be represented as the following functions of the minimum principal stress σ_3 and the maximum principal stress σ_1 :

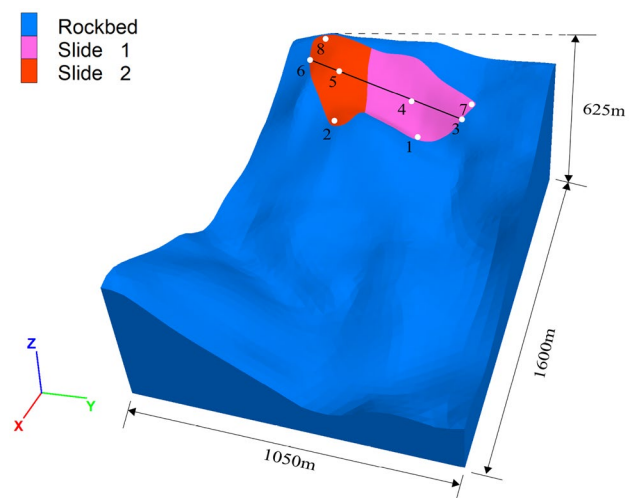


Fig. 13 FDM-based simulation model and monitoring points

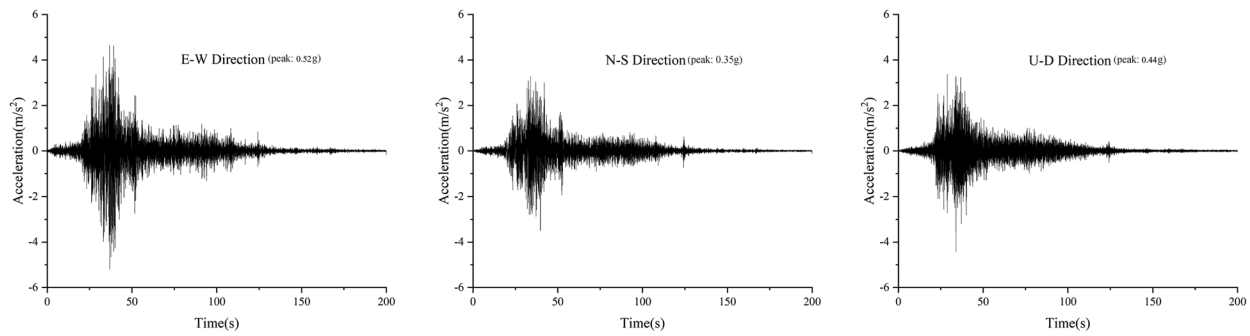


Fig. 14 Acceleration records from a seismograph station in Hanzeng town, 64 km away from the WRA. The peak accelerations were 0.519, 0.350, and 0.444 g in the EW, NS, and vertical directions, respectively

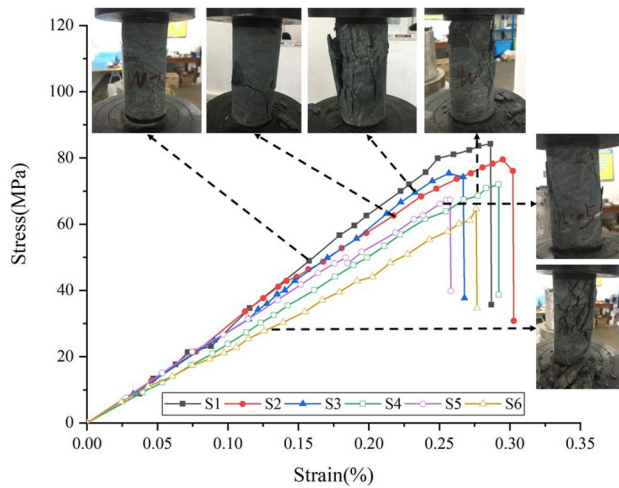


Fig. 15 Fracture localization and flying fragments of brittle limestone under uniaxial compression

$$\tau = \frac{1}{2}(\sigma_1 - \sigma_3) \cos \varphi \quad (1)$$

$$\sigma = \frac{1}{2}(\sigma_1 + \sigma_3) + \frac{1}{2}(\sigma_1 - \sigma_3) \sin \varphi \quad (2)$$

According to the Coulomb failure criterion ($\tau = c + \sigma \tan \varphi$), the element will cause shear failure while the stress condition ($\sigma_1 - \sigma_3 N_\varphi + 2c \sqrt{N_\varphi} = 0$) (Fig. 16). According to the maximum

tensile stress criterion, the element will cause tensile failure while the stress condition ($\sigma_1 - \sigma_3 = 0$) (Fig. 16).

Eight monitoring points were set on the source areas to record the velocities, displacements and maximum shear strain increments of the original slope under the seismic accelerations. Due to the time-consuming calculation of the large-volume multi-grid model, the running was ceased after significant deformation of the source.

The displacements and maximum shear strain increments of the WRA during the earthquake are illustrated in Figs. 17, 18, and 19. With seismic waves propagating in the model, the displacements increase gradually from the toe to the rear of the source I. When t reaches 6 s, the displacements of the sources I and II were 34 m and 0 m (Fig. 17b), the maximum principal strain increments were 67% and 0% (Fig. 18b), respectively. Moreover, the obvious shear crack at the front and tensile crack at the rear of the source I appeared, the source completely disintegrated and began to move on a large scale (Figs. 17b and 18b). When t reaches 30 s, the maximum displacement of the sliding source I approximates 208 m (Fig. 17f).

As shown in the Fig. 19, the shear displacement of the sliding plane under the source I rapidly increased from 5.3 m at the $t = 2$ s to 149.1 m at $t = 30$ s, in which the one under the source II slowly increased. The ruptures at the main scarp and the left margin firstly occurred at $t = 2$ s (Fig. 19a). By comparing the shear deformation degree of different areas of the sliding surface, it can be seen that the source I initially destabilized and rapidly slid, but the source II deformed slightly.

According to the accumulative displacements and maximum strain increments of the monitoring points (Figs. 20 and 21), the source I represented by the monitoring points 1, 3, 4 and 7 totally destabilized and the source II represented by the monitoring points 2, 5, 6 and 8 slightly deformed till 30 s. The results indicated that the

Table 2 Physical and mechanical parameters of the bedrock, sliding masses and sliding plane

| Lithology | Density (kg/m ³) | Elasticity modulus (GPa) | Poisson rate | Internal friction angle (°) | Cohesion (kPa) | Normal stiffness (MPa/m) | Shear stiffness (MPa/m) |
|----------------|------------------------------|--------------------------|--------------|-----------------------------|----------------|--------------------------|-------------------------|
| Sliding masses | 2600 | 30 | 0.30 | 35 | 10 | | |
| Bedrock | 2600 | 60 | 0.22 | 50 | 50 | | |
| Sliding plane | | | | 15 | 10 | 100 | 100 |

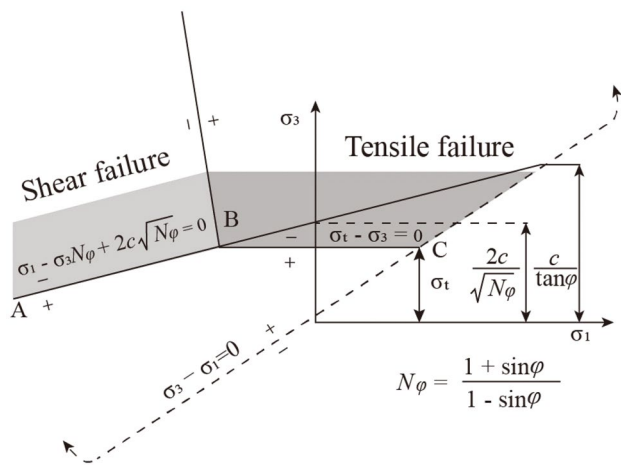


Fig. 16 Schematic diagram of Mohr–Coulomb failure criterion (Itasca Consulting Group, Inc 2018)

deep-cutting gully provides enough motional space for sliding and the ridge act as a barrier. Moreover, the sliding plane of the source I dipping outward the slope and the sliding plane of the source II dipping inward slope play a crucial effect on the failure process.

Discussion

Coupling effect of the alpine-gorge topography, co-seismic surface rupture and brittle carbonate strata on earthquake-induced rockslide

The combined condition of the alpine-gorge topography with deep-incised gullies, carbonate bedrock with brittle failure characteristic and strong seismic loading concentrating along the co-seismic

surface rupture should be responsible for the catastrophic Woqian rockslide avalanche. The undercut and retrogressive erosion of the runoff from the long-term precipitation in the catchment area of the gully could expose the unfavorable structural planes and deteriorate the quality of the carbonate bedrock. In addition, the strain energy stored in rock masses was released centrally along the co-seismic surface rupture that can cause the seismic waves amplification to the nearby slopes (Kargel et al. 2016).

Accordingly, the spatial distribution characteristics of co-seismic landslides triggered by the M 7.9 Wenchuan earthquake, M 7.0 Lushan earthquake and M 7.0 Jiuzhaigou earthquake in southwest China, the rockslides concentrated in carbonate rocks (Gorum et al. 2010; Chang et al. 2021). This can be attributed to the generated dissolved cracks by the long-term precipitation and the brittle failure characteristics of carbonate rocks (Gorum et al. 2011; Vanani et al. 2021).

After the Wenchuan earthquake, as of June 16, 2022, 13 earthquakes of magnitude > 6.0 have occurred along the Longmenshan seismogenic fault (data from China Earthquake Administration). In the southwestern region of the Longmenshan seismogenic fault, the M 6.1 Lushan earthquake and the M 4.5 Baoxing earthquake happened at 3-min intervals on 1 June 2022. In addition, ten earthquakes with a maximum magnitude of 6.0 and a minimum of 3.0 occurred in Maerkang City on June 10, 2022, which is the intersection region of Longmenshan fault and Xianshuihe fault. The Qinchuan fault, as the northeastern branch of the Longmenshan seismogenic fault, has a high possibility to reactivate and cause earthquakes in the future. In addition, the long-term effects of the previous earthquakes, involving the shatter effect and strength deterioration effect will continue to affect the stability of slopes. Therefore, the risk of new landslides in strong earthquakes areas as the main engineering geological problems in Sichuan still needs continuous attention.

Through the case study, the generalized conclusion that the carbonate strata in gully catchment area near the fault is the highest

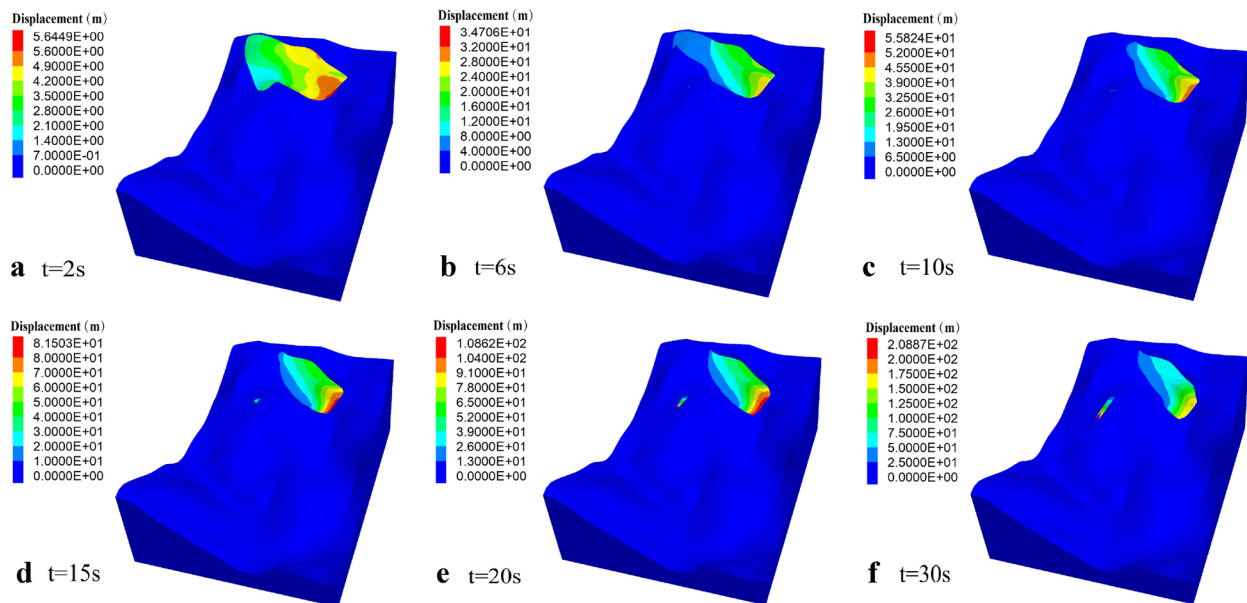


Fig. 17 Contours of the displacements of the sliding masses

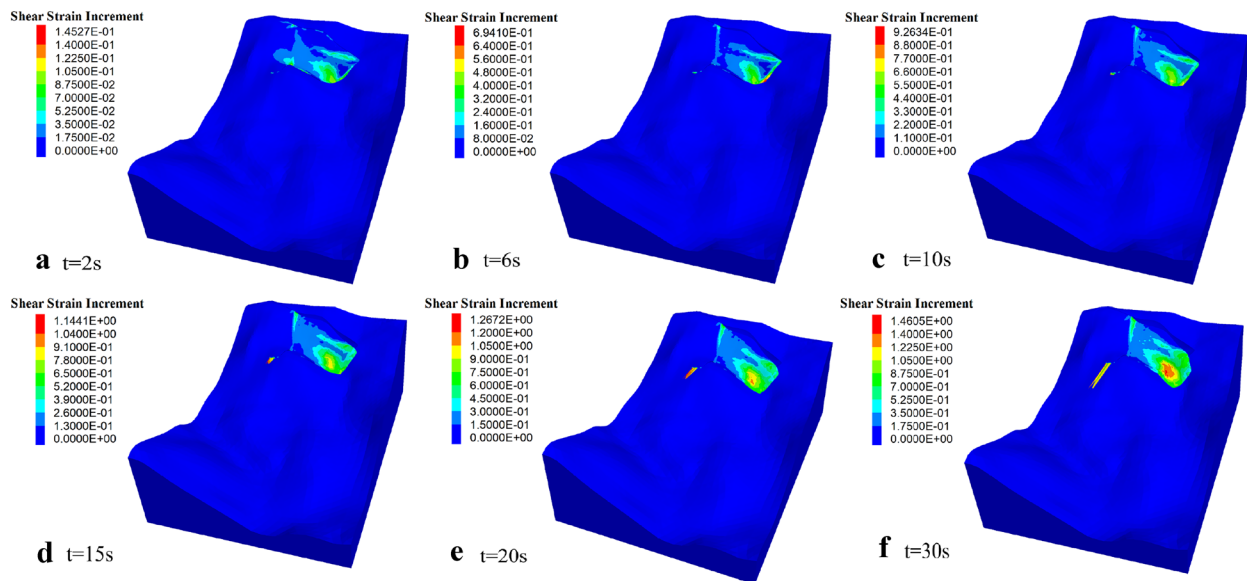


Fig. 18 Contours of the shear strain increments of the sliding masses at different time steps

risk area of earthquake-induced landslides was proposed, which will enable to deepen the understanding of other researchers and practitioners.

Initiation mechanism of the WRA

Because the deep-undercutting ditches reduced the lateral restraint and partly uncovered the unconformity contact plane within the strata, the slope could continuously deform and creep in the past. Due to the strong seismic loading, the shear stress rapidly increased more than the shear strength of the sliding plane at the bottom

of the source I and tension cracking occurred at the slope scarp (Fig. 18). Then, the source initially destabilized and slid. The geo-mechanical mode of the deformation and failure of the WRA was sliding tension-shear failure.

After the source I as a resisting key block sliding away and producing a new cliff, the source II caused an apparent dip sliding along the inward inclined bedding plane of the limestone. Normally, the apparent dip sliding rockslides are rare but could occur after the failure of the “key resistance block” under strong earthquake or artificial excavation (Zhang et al. 2016, 2019). Therefore, the delayed failure and secondary collapse of the main scarp should be kept in mind for the

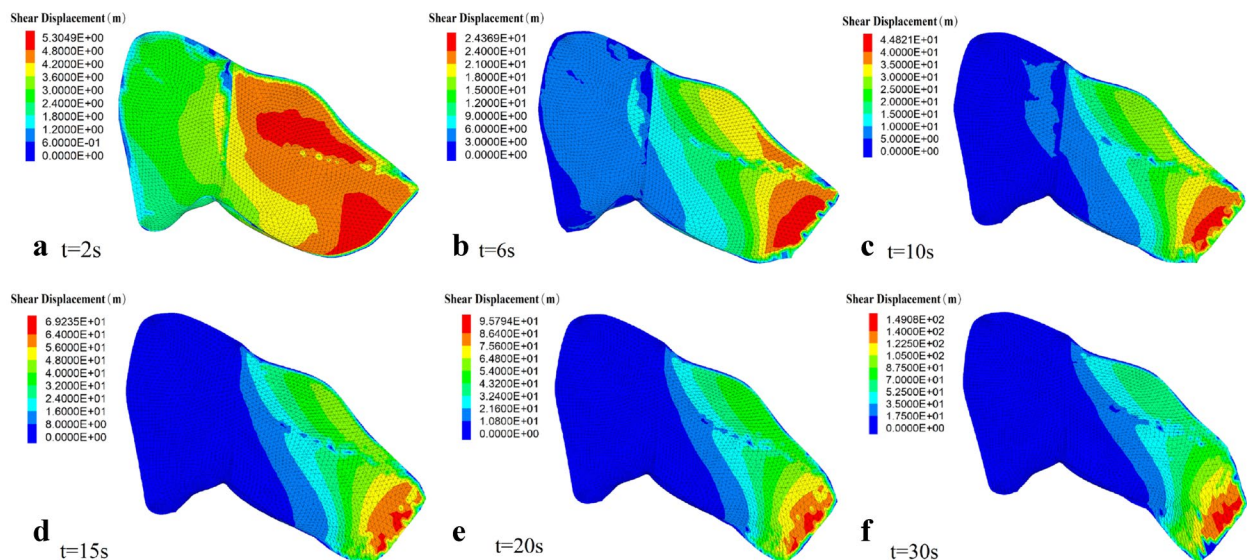


Fig. 19 Accumulative shear displacements of the sliding plane at different time steps

Fig. 20 Accumulative displacements of the monitoring points

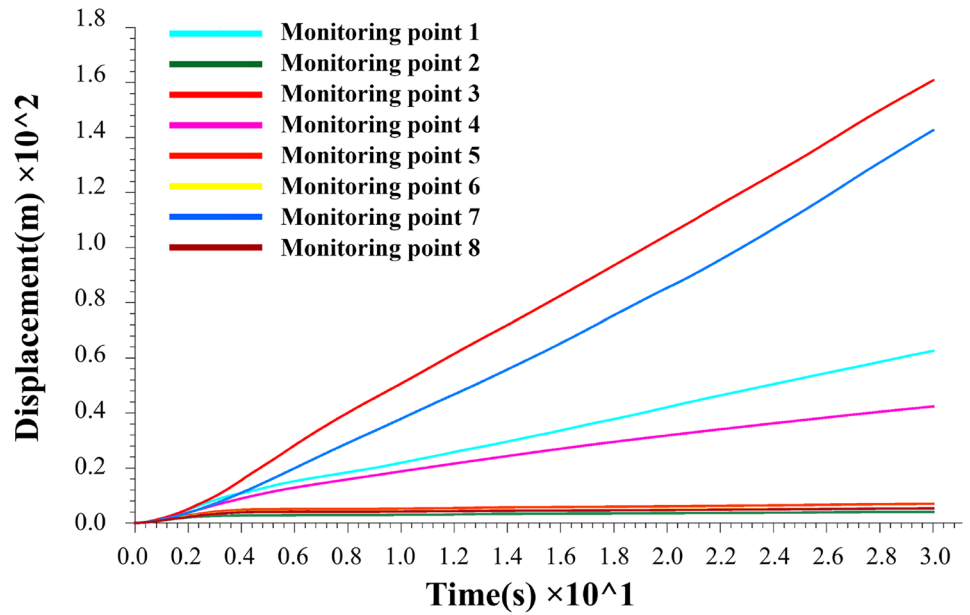
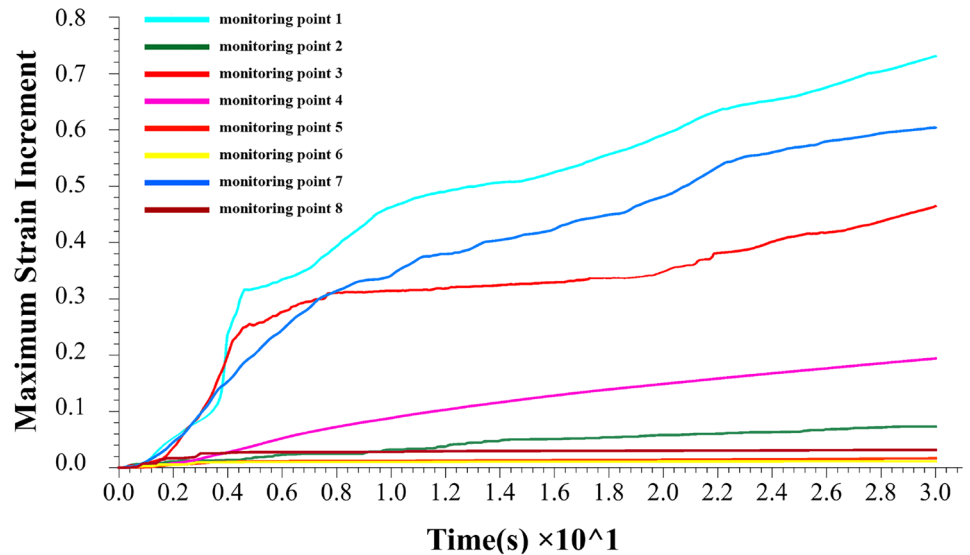


Fig. 21 Maximum strain increments of the monitoring points



emergency rescue workers. However, accurately predicting the destabilization time and collapse scale is still a challenging issue (Chang et al. 2022), requiring advances in remote monitoring technologies and artificial intelligence optimization algorithms for slope instability analysis (Matsuoka 2019; Gong 2021; He et al. 2022).

Role of the numerical methods on the failure mechanism of rockslides

The state-of-the-art numerical simulation methods can investigate the progressive failure process and help us to predict risk region. However, the accurate results with satisfactory precision depend on multi-variables, such as the high-resolution DEM, clear location and geomorphology of the sliding plane, reasonable physical

and mechanical parameters of rock masses, suitable constitutive model and fracture criterion. Verifying the precision of the simulated results was a very difficult task and needed enormous field data. According to the newly generated grooves, the step-shaped sliding planes and sedimentary characteristics of the deposits, the simulated results by FLAC_{3D} was receivable.

Conclusion

1. The Woqian rockslide was directly triggered by the seismic force of the Wenchuan earthquake and transformed as a high-speed and long-runout rock avalanche. Based on the evidences of the different inclination striations on the exposed bedrock in the main scarp, the discontinuous step-shaped sliding

planes, the two newly generated grooves, the topography characteristics of the deposits, the failure mechanism of the WRA was determined as twice destabilizations of the sources in tandem. The impact-induced fragmentation between the sliding masses and the banks and the shear-induced fragmentation between the sliding masses and the ground are the most probable mechanism that can adequately explain the characteristics of the rock avalanche deposit.

2. The simulation results using FLAC3D indicates that when the earthquake reaches 6 s, the shear strain increment and displacement of the source I was very large and the obvious shear crack at the front and tensile crack at the rear appeared. The results manifested that the source I was firstly destabilized during the earthquake and source II failed after the sliding of source I. The special twice destabilizations of the WRA can provide new insight into the brittle fracture mechanism of earthquake-induced landslides and will guide the prevention and mitigation of the landslides.
3. The carbonate rock slopes in the catchment area of the eroded sinuous gully near the active faults are areas prone to huge-volume catastrophic rockslides under a strong earthquake. Moreover, the subsequent failure after the first rockslide and secondary collapse of the main scarp during the future earthquakes should be paid more attention during the geological investigations, risk assessments, rescue and mitigation works as well as the site selection of infrastructures.

Acknowledgements

The authors would like to acknowledge the Sichuan Province Science and Technology Support Program (2021YJ0033) and the research project of the Department of Natural Resources of Sichuan Province (Kj-2022-29) for their strong support for this topic. The authors would like to express their sincere gratitude to Professor Bernd Wünnemann of Southwest Jiaotong University for discussing the academic ideas and improving the quality of the paper. Further, the authors also thank the anonymous reviewers for their valuable time and suggestions.

Declarations

Competing interests The authors declare no competing interests.

References

- Chang M, Cui P, Xu L, Zhou Y (2021) The spatial distribution characteristics of coseismic landslides triggered by the Ms7.0 Lushan earthquake and Ms7.0 Jiuzhaigou earthquake in southwest China. *Environ Sci Pollut Res* 28(16):20549–20569. <https://doi.org/10.1007/s11356-020-11826-5>
- Chang WB, Xu Q, Dong XJ, Zhuang Y, Xing AG, Wang Q, Kong, X.Z. (2022) Dynamic process analysis of the Xinmo landslide via seismic signal and numerical simulation. *Landslides* 19(6):1463–1478. <https://doi.org/10.1007/s10346-022-01876-w>
- Cui SH, Pei XJ, Jiang Y, Wang GH, Fan XM, Yang QW, Huang RQ (2021) Liquefaction within a bedding fault: understanding the initiation and movement of the Daguangbao landslide triggered by the 2008

- Wenchuan Earthquake (Ms=8.0). *Eng Geol* 295:106–455. <https://doi.org/10.1016/j.enggeo.2021.106455>
- Dai FC, Tu XB, Xu C, Gong QM, Yao X (2011) Rock avalanches triggered by oblique-thrusting during the 12 May 2008 Ms 8.0 Wenchuan earthquake, China. *Geomorphology* 132:300–318. <https://doi.org/10.1016/j.geomorph.2011.05.016>
- Fan XM, Scaringi G, Korup O, West AJ, Westen CJ, Tanyas H, Hovius N, Hales TC, Jibson RW, Allstadt KE, Zhang LM, Evans SG, Xu C, Li G, Pei XJ, Xu Q, Huang RQ (2019) Earthquake-induced chains of geologic hazards: patterns, mechanisms, and impacts. *Rev Geophys* 57(2):421–503. <https://doi.org/10.1029/2018RG000626>
- Gombert B, Duputel Z, Shabani E, Rivera L, Jolivet R, Hollingsworth J (2019) Impulsive source of the 2017 $M_w=7.3$ Ezgeleh, Iran, earthquake. *Geophys Res Lett* 46(10):5207–5216. <https://doi.org/10.1029/2018GL081794>
- Gong B (2021) Study of PLSR-BP model for stability assessment of loess slope based on particle swarm optimization. *Sci Rep* 11(1):1–10. <https://doi.org/10.1038/S41598-021-97484-0>
- Gong B, Tang CA (2017) Slope-slide simulation with discontinuous deformation and displacement analysis. *Int J Geomech* 17(5):E4016017
- Gorum T, Fan XM, Van Western CJ, Huang RQ, Xu Q, Tang C, Wang GH (2011) Distribution pattern of earthquake-induced landslides triggered by the 12 May 2008 Wenchuan earthquake. *Geomorphology* 133:152–167. <https://doi.org/10.1016/j.geomorph.2010.12.030>
- He K, Ma G, Hu X (2021) Formation mechanisms and evolution model of the tectonic-related ancient giant basalt landslide in Yanyuan County, China. *Nat Hazards* 106:2575–2597. <https://doi.org/10.1007/s11069-021-04555-6>
- He K, Liu B, Hu X, Zhou R, Xi C, Ma G, Han M, Li Y, Luo G (2022) Rapid characterization of landslide-debris flow chains of geologic hazards using multi-method investigation: case study of the Tiejiangwan LDC. *Rock Mech Rock Eng*. <https://doi.org/10.1007/s00603-022-02905-9>
- Huang Y, Zhang B, Zhu CQ (2021) Computational assessment of baffle performance against rapid granular flows. *Landslides* 18:485–501. <https://doi.org/10.1007/s10346-020-01511-6>
- Hungr O (2006) Rock avalanche occurrence, process and modelling. *Landslides from massive rock slope failure*. *Landslides* 49:243–266. https://doi.org/10.1007/978-1-4020-4037-5_14
- Hungr O, Leroueil S, Picarelli L (2014) The Varnes classification of landslide types, an update. *Landslides* 11:167–194. <https://doi.org/10.1007/s10346-013-0436-y>
- Itasca Consulting Group, Inc (2018) *Fast Lagrangian Analysis of Continua*, ver. 6.0 Manual. Itasca, Minneapolis
- Kargel JS, Leonard GJ, Shugar DH (2016) Geomorphic and geologic controls of geo-hazards induced by Nepal's 2015 Gorkha earthquake. *Science* 351(6269):1–18. <https://doi.org/10.1126/science.aac8353>
- Keefer DK (1984) Landslides caused by earthquakes. *Geol Soc Am Bull* 95(4):406–421. [https://doi.org/10.1130/0016-7606\(1984\)95%3c406:LCBE%3e2.0.CO](https://doi.org/10.1130/0016-7606(1984)95%3c406:LCBE%3e2.0.CO)
- Liu B, Hu X, He K, He S, Shi H, Liu D (2020) The starting mechanism and movement process of the coseismic rockslide: a case study of the Laoyingyan rockslide induced by the “5.12” Wenchuan earthquake. *J Mt Sci* 17(5):1188–1205. <https://doi.org/10.1007/s11629-019-5775-2>
- Lin C, Pastor M, Li T, Liu X, Qi H, Lin C (2019) A SPH two-layer depth-integrated model for landslide-generated waves in reservoirs: application to Halaowo in Jinsha River (China). *Landslides* 16(11):2167–2185. <https://doi.org/10.1007/s10346-019-01204-9>
- Lin F, Wu LZ, Huang RQ, Zhang H (2018) Formation and characteristics of the Xiaoba landslide in Fuquan, Guizhou, China. *Landslides* 15:669–681. <https://doi.org/10.1007/s10346-017-0897-5>
- Mahani AB, Kazemian J (2018) Strong ground motion from the November 12, 2017, M7.3 Kermanshah earthquake in western Iran. *J Seismol* 22(6):1339–1358. <https://doi.org/10.1007/s10950-018-9761-x>
- Matsuoka N (2019) A multi-method monitoring of timing, magnitude and origin of rockfall activity in the Japanese Alps. *Geomorphology* 336:65–76. <https://doi.org/10.1016/j.geomorph.2019.03.023>
- Oswald P, Strasser M, Hammerl C, Moernaut J (2021) Seismic control of large prehistoric rockslides in the Eastern Alps. *Nat Commun* 12(1):1059–1066. <https://doi.org/10.1038/s41467-021-21327-9>
- Petley DN (2013) Characterizing giant landslides. *Science* 339(6126):1395–1396. <https://doi.org/10.1126/science.1236165>

- Pudasaini SP, Miller SA (2013) The hypermobility of huge landslides and avalanches. *Eng Geol* 157:124–132. <https://doi.org/10.1016/j.enggeo.2013.01.012>
- Qi SW, Xu Q, Lan HX, Zhang B, Liu JY (2010) Spatial distribution analysis of landslides triggered by 2008.5.12 Wenchuan earthquake, China. *Eng Geol* 116:95–108. <https://doi.org/10.1016/j.enggeo.2010.07.011>
- Roback K, Clark MK, West AJ, Zekkos D, Li G, Gallen SF, Chamlagain D, Godt JW (2018) The size, distribution, and mobility of landslides caused by the 2015 Mw7.8 Gorkha earthquake. *Nepal Geomorphology* 301:121–138. <https://doi.org/10.1016/j.geomorph.2017.01.030>
- Stead D, Wolter A (2015) A critical review of rock slope failure mechanisms: the importance of structural geology. *J Struct Geol* 74:1–23. <https://doi.org/10.1016/j.jsg.2015.02.002>
- Sun HY, He HL, Ikeda Y, Kano K, Shi F, Gao W, Echigo T, Okada S (2015) Holocene paleoearthquake history on the Qingchuan fault in the northeastern segment of the Longmenshan thrust zone and its implications. *Tectonophysics* 660:92–106. <https://doi.org/10.1016/j.tecto.2015.08.022>
- Sun P, Zhang YS, Shi JS, Chen LW (2011) Analysis on the dynamical process of Donghekou rockslide-debris flow triggered by 5.12 Wenchuan earthquake. *J Mt Sci* 8:140–148. <https://doi.org/10.1007/s11629-011-2112-9>
- Tang MG, Xu Q, Zhang W (2011) Discuss on failure mechanism and geologic characteristic of Woqian landslide triggered by Wenchuan earthquake. *Chin J Rock Mech Eng* 30(52):3491–3502 (in Chinese)
- Vanani AAG, Shoaei G, Zare M (2021) Statistical analyses of landslide size and spatial distribution triggered by 1990 Rudbar-Manjil (Mw 7.3) earthquake, northern Iran: revised inventory, and controlling factors. *Bull Eng Geol Env* 80:3381–3403. <https://doi.org/10.1007/s10064-021-02106-8>
- Wang GH, Huang RQ, Chigira M, Wu XY, Lourenço SD (2013) Landslide amplification by liquefaction of runout-path material after the 2008 Wenchuan (M 8.0) earthquake, China. *Earth Surf Process Landf* 38(3):265–274. <https://doi.org/10.1002/esp.3277>
- Wang HL, Liu SQ, Xu WY, Yan L, Qu X, Xie WC (2020) Numerical investigation on the sliding process and deposit feature of an earthquake-induced landslide: a case study. *Landslides* 17:2671–2682. <https://doi.org/10.1007/s10346-020-01446-y>
- Wang T, Wu SR, Shi JS, Xin P, Wu LZ (2018) Assessment of the effects of historical strong earthquakes on large-scale landslide groupings in the Wei River midstream. *Eng Geol* 235:11–19
- Wang WP, Yin YP, Zhu SN, Wang LC, Zhang N, Zhao RX (2019a) Investigation and numerical modeling of the overloading-induced catastrophic rockslide avalanche in Baige, Tibet, China. *Bull Eng Geol Env* 79(4):1765–1779. <https://doi.org/10.1007/s10064-019-01664-2>
- Wang XL, Clague JJ, Crosta GB, Sun JJ, Stead D, Qi SW, Zhang LQ (2021) Relationship between the spatial distribution of landslides and rock mass strength, and implications for the driving mechanism of landslides in tectonically active mountain ranges. *Eng Geol* 292:106281. <https://doi.org/10.1016/j.enggeo.2021.106281>
- Wang YF, Cheng QG, Zhu Q (2015) Surface microscopic examination of quartz grains from rock avalanche basal facies. *Can Geotech J* 52(2):167–181. <https://doi.org/10.1139/cgj-2013-0284>
- Wang YS, Wu LZ, Gu J (2019b) Process analysis of the Moxi earthquake-induced Lantianwan landslide in the Dadu River, China. *Bull Eng Geol Env* 78:4731–4742. <https://doi.org/10.1007/s10064-018-01438-2>
- Xu C, Xu XW (2014) Statistical analysis of landslides caused by the Mw 6.9 Yushu, China, earthquake of April 14, 2010. *Nat Hazards* 72(2):871–893. <https://doi.org/10.1007/s11069-014-1038-2>
- Xu C, Xu XW, Yao X, Dai FC (2014) Three (nearly) complete inventories of landslides triggered by the May 12, 2008 Wenchuan Mw 7.9 earthquake of China and their spatial distribution statistical analysis. *Landslides* 11(3):441–461. <https://doi.org/10.1007/s10346-013-0404-6>
- Yin YP, Li B, Wang WP (2015) Dynamic analysis of the stabilized Wangjiayan land-slide in the Wenchuan Ms 8.0 earthquake and aftershocks. *Landslides* 12:537–547. <https://doi.org/10.1007/s10346-014-0497-6>
- Zhang M, Yin YP, Mcsaveney M (2016) Dynamics of the 2008 earthquake-triggered Wenjiagou Creek rock avalanche, Qingping, Sichuan, China. *Eng Geol* 200:75–87. <https://doi.org/10.1016/j.enggeo.2015.12.008>
- Zhang M, Wu LZ, Zhang JC, Li LP (2019) The 2009 Jiweishan rock avalanche, Wulong, China: deposit characteristics and implications for its fragmentation. *Landslides* 16:893–906. <https://doi.org/10.1007/s10346-019-01142-6>
- Zhang SL, Yin YP, Hu XW, Wang WP, Li ZL, Wu XM, Luo G, Zhu SN (2021) Geostuctures and deformation-failure characteristics of rockslide areas near the Baige landslide scar in the Jinsha River tectonic suture zone. *Landslides* 18(11):3577–3597. <https://doi.org/10.1007/s10346-021-01741-2>

Springer Nature or its licensor holds exclusive rights to this article under a publishing agreement with the author(s) or other rightsholder(s); author self-archiving of the accepted manuscript version of this article is solely governed by the terms of such publishing agreement and applicable law.

Gang Luo (✉) · **Xinan Chen** · **Qian Zhang** · **Kun He** · **Maolin Wu** · **Weigang Shen** · **Bo Liu**

Faculty of Geosciences and Environmental Engineering, Southwest Jiaotong University, Chengdu 610031, China
Email: luogang@home.swjtu.edu.cn